JEE Journal of Ecological Engineering

*Journal of Ecological Engineering* 2024, 25(8), 99–118
https://doi.org/10.12911/22998993/189862
ISSN 2299–8993, License CC-BY 4.0

Received: 2024.05.23
Accepted: 2024.06.17
Published: 2024.07.01

# Synthesis and Characterization of Novel Biochar Developed from Peganum Harmala Seeds to Adsorb Heavy Metals from Aqueous Solution

Douha Sabah Khudair[1*], Yasser I. Abdulaziz[1]

[1] Department of Chemical Engineering, Al Nahrain University, Baghdad, Iraq

* Corresponding author's email: douha.mche23@ced.nahrainuniv.edu.iq

## ABSTRACT

Referring to the oil and industrial development, contamination of water streams and soil by heavy metals becomes severe issue. Biochar has consider as cheap and ecofriendly adsorbent for heavy metal ions removal. As well as, the development and modification of biochar has been a center point of many researches. In this study it has been suggested to develop novel biochar from Peganum harmala seed precursor and evaluate the heavy metal ions adsorption performance. Chemical activation process was adopted to prepare biochar with different concentrations (20%, 30%, and 40%) of phosphoric acid followed by pyrolysis in a laboratory horizontally tube furnace underneath an $N_2$ blanket at 600 °C for 3 hours. The physical and chemical properties of biochar have been assessed using Energy Dispersive X-ray Spectroscopy, X-ray diffraction, Scanning Electron Microscopy, pore structure, and Fourier-transform analysis. The prepared biochar was investigated to absorb three different heavy metal ions Fe(III), Ni(II) and Pb(II) from an aqueous solution under varied conditions. Heavy metal concentration (20–100 ppm), adsorbent dosage (0.25–0.75) g/L, contact duration (0–560 min), and solution pH (2–9) were examined. The results show that the largest BET surface area (691.58 $m^2/g$) was achieved with activation conversation of 40% $H_3PO_4$ and 600 °C for 3 hours, compared to other samples. The maximum adsorption capacities were 113.4096, 112.3355, 180.3478 mg/g for Fe(III), Ni(II) and Pb(II) respectively. Finally, Freundlich isotherm model shows better describe the adsorption equilibrium data, while adsorption kinetic data shows the pseudo-first-order model fits more with Fe(III) ions which shows that chemisorption was controlled in the adsorption process, additionally the pseudo-first-order model fits more with Pb(II) and Ni(II) ions this mean the physisorption has been controlled in the adsorption process.

**Keywords:** biochar; Peganum harmala seeds; adsorption; heavy metal ions; kinetic isotherm models.

## INTRODUCTION

Contamination of water sources by heavy metal ions such as $Cd^{+2}$, $Cu^{+2}$, $Pb^{+2}$, $Fe^{+2}$, $Ni^{+2}$, $Zn^{+2}$ and others is a major cause for concern because of the destructive effects causes on ecosystems and the health of humans (El-Bendary *et al*., 2021; Alslaibi *et al.*, 2014). Generally, human activities, oil processes, and industries are the main sources for contaminating the underground and surface water with heavy metal ions (Brishti *et al.*, 2023). The removal of heavy metal ions from wastewater has been the topic of much investigation using physical and chemical approaches such as chemical precipitation (Kannan and Mani, 2014), adsorption (Ammar and Jaafar, 2017), flotation (Taseidifar *et al.,* 2017), biosorption (Slaiman, Haweel and Abdulmajeed, 2010), ultrafiltration (Mungray *et al*., 2012), electrochemical techniques (Radhy and Najim, 2022), and coagulation (Mousa and Hadi, 2016). Adsorption is considered to be more successful for a range of applications than other remediation procedures, as the other approaches have constraints and limitations. Organic dyes, dangerous substances such as phenol, pesticides, and cyanides are only some of the soluble organic contaminants that may be effectively removed using adsorption (Adib *et al.*, 2017). Common adsorbent materials include activated carbon has many benefits that make it a

popular adsorbent in water treatment, alongside zeolites, silica gels, aluminas, and resins referring to porous structure, high specific surface area, thermal and chemical stable, and ability to remove A wide range of contaminants (Elmaguana *et al.*, 2018) (Amer *et al.*, 2021). Nowadays, activated carbon are wildly produced from agricultural biomass as a raw material, thanks to its availability, risk free, renewability and low cost such as coffee ground (Zainab Alaa Hassan Ali, 2024), peanut hulls (Girgis et al., 2002), reedy grass leaves (Xu *et al.*, 2014), durian shell (Chandra *et al.*, 2009), *Glebionis coronaria* L. (Tounsadi et al., 2016), Diplotaxis harra (Tounsadi, Khalidi, Abdennouri, *et al.*, 2016), Phanera vahlii fruit's (Ajmani *et al.*, 2020), Imperata (Abdulmajeed et al., 2018), sunflower oil cake (Karagöz *et al.*, 2008).

Chemical and physical activation techniques are the two main methods for preparing activated carbons from biomass. In physical activation, a carbonaceous substance is first carbonized and then activated at high temperatures with the help of oxidizing gases such steam, air, carbon dioxide, or a mixture of these (Yang *et al.*, 2010). Pyrolyzing is the last step in chemical activation which involve (Jun *et al.*, 2010) impregnating the precursor with a specific chemical agent (Lozano-Castello *et al.*, 2001). In the carbonization process, activating agents such as $ZnCl_2$, $H_3PO_4$, KOH, $K_2CO_3$, and $Na_2CO_3$ were used (Shrestha and Nyachhyon, 2021). One benefit of chemical activation versus physical activation is that it just takes one step and acts at a lower temperature.. Moreover, chemical activation lowered the quantity of mineral matter and yields much more than physical activation. However, there are a few downsides to the chemical activation approach, including the fact that it is corrosive and that cleaning is a pain (Timur *et al.*, 2010).

Chars and coal precursors are activated using metal compounds like potassium hydroxide; whereas lignocellulosic materials that have not been carbonized before are activated using phosphoric acid and zinc chloride (Prahas *et al.*, 2008). Phosphoric acid is favored over zinc chloride due to the environmental implications of the latter. Additionally, it is linked to issues of corrosion and ineffective chemical recovery. In addition, the carbon that is obtained via zinc chloride should not be used in the food and pharmaceutical sectors due to the possibility of pollution (Yakout and Sharaf El-Deen, 2016)

The present study is focused to synthesis high surface area biochar developed from peganum harmala seeds as a potential new source of material. It has been noted that these seeds are rich in carbon contained, locally available, very cheap and ecofriendly. Moreover, the removal efficiency of the prepared biochar by chemical activation method has to be evaluated for remediation of heavy metal ions $Fe^{+3}$, $Ni^{+2}$, and $Pb^{+2}$ from simulated aqueous media through adsorption under various operating conditions.

## MATERIAL AND METHODS

### Materials

Biomass (Peganum harmala seeds – Pgh) sample was obtained from a community market. Calderoni et al. (2021) deeply investigate Peganum harmala seeds. The chemical components that were found by EDX analysis of Pgh are shown in Table 2, and Table 1 explains the chemicals used in this work.

### Biochar preparation

Pgh seeds were utilized to prepare biochar (BC). Primarily they were washed with tap water several times to remove dust and other undesired materials, then with distilled water to remove

**Table 1.** The chemicals that were used in the work

| Chemicals used in the workplace | Chemical formula | Purity | The origin |
|---|---|---|---|
| Phosphoric acid | ($H_3PO_4$) | 85% | UK |
| Hydrochloric acid HCl | (HCl) | 35–38% | Germany |
| Sodium hydroxide | (NaOH) | 97% | Germany |
| Ferric chloride | (FeCl3) | 97% | India |
| Nickel chloride | (NiCl2) | 98% | India |
| Lead nitrate | $Pb(NO_3)_2$ | 99% | India |
| Deionized water | H2O | 100% | Iraq |

**Table 2.** The chemical components for Peganum harmala seeds

| Element | Atomic % | Weight % |
|---|---|---|
| C | 58.1 | 49.3 |
| O | 40.1 | 45.3 |
| Mg | 0.3 | 0.4 |
| Cl | 0.2 | 0.5 |
| K | 0.2 | 0.6 |
| Ca | 0.5 | 1.5 |
| Fe | 0.1 | 0.3 |
| Ni | 0.2 | 0.8 |
| Zn | 0.3 | 1.2 |

foreign elements. Followed, dried for 24 hours in an electric oven at 105 °C. After that, the clean dried seeds were crushed using electric herb grain grinder and sieved to achieve (1–1.18) mm grain size.

Twenty grams of Pgh was soaked with a 50 mL of 20, 30, and 40% $H_3PO_4$ solution and kept in a water-bath at 80 °C for 24 h until the extra solution evaporated. It has been noticed that it took longer time to evaporate the impregnated samples' surplus solution depending on the quantity of $H_3PO_4$ employed for activation. Also, the drying time increased with activating agent concentration. Oven-dried samples were carbonized in tubular electric furnace (GSL 1600X - China) at 600 °C for three hours using nitrogen gas flow rate of 100 $cm^3$/min (Aljumaili and Abdul-Aziz, 2023). Started by heating the impregnated sample at rate of heat 10 °C/min from room temperature to the desired carbonization temperature was obtained. The samples supposed to still at 600 °C for 3 hours. After all, the cooled samples were washed with deionized water and then dried overnight in an electrical heater to achieve biochar ready to use. shows steps of preparing BC.

## Biochar properties

The surface areas of the resulting samples were calculated using SA-9600 Qsurf series model Surface Area Analyzer (BET test, Thermo Electron Corporation). The diagnostic evaluation of the surface morphologies was performed utilizing a scanning electron microscope (Thermo Fisher Scientific). FT-IR analysis (Bruker Alpha) was employed to ascertain the chemical properties within the scanned range of 4000 to 400 $cm^3$. Utilizing EDX (HRSEM FEI Inspect F50), the combination of chemical elements of the raw martial and AC that was prepared was ascertained. Using XRD (Panalytical) with Cu Ka radiation (= 0.154 nm), a fixed power supply of 40 kilovolts and 30 microamperse-seconds, with a step size of 0.05° in the 2 theta range from 10 to 80° (high angle), the identity of the prepared BC was determined. The Matlab program was utilized to characterize the surface physical properties.

## Study of batch adsorption

Studies of batch adsorption were performed to investigate the removal adsorption percent of $Fe^{+3}$, $Ni^{+2}$, and $Pb^{+2}$ using BC sample that has highest surface area. Several variables

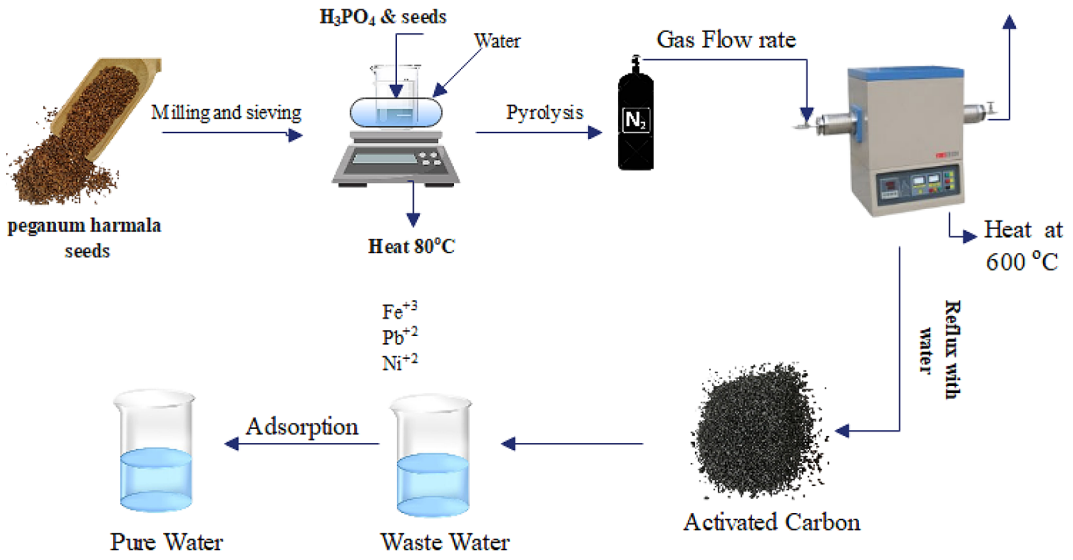


**Figure 1.** The steps involved in making biochar

have been studied on the adsorption process such as heavy metals initial concentration, pH of solution, exposure time and adsorbent material dose. It is essential to note that these tests were carried out utilizing a factorial model, which keeps the other variables fixed and only modifies one variable at a time.

First, the stock solution has been prepared with a maximum heavy metal ion concentration of 1000 ppm. This has been achieved by dissolving 2.818 g of ferric chloride ($FeCl_3$), 1.5985 g of lead nitrate $Pb(NO_3)_2$ and 4.0497 g of nickel chloride ($NiCl_2$) in 1000 ml de-ionized distilled water. The desired concentrations of heavy metal ion pollutants (20, 50, and 100 mg/L) was obtained by diluting the stock solution. To establish sorption equilibrium, 0.5g/L of synthesized BC was shaken into 150 mL of simulated solutions at surroundings temperature (25 ± 2 °C) and pH 7 for 440 minutes. Numerous samples have been withdrawn from the solution using micropipette and filtered at almost equal intervals from 5 to 560 minutes. The absorbance of solutions is analyzed using an Atomic Absorption Spectrometer (AAS) (Analytik Jena, Germany). The capacity of the adsorbed ions (qe) (mg/g) was estimated by Equation 1:

$$qe = (Co - Ce) \times \frac{V}{M} \tag{1}$$

The percentage $R$% of adsorption removal calculated using Equation 2:

$$R\% = \frac{(Co-Ce)}{Co} \times 100\% \tag{2}$$

where: $C_0$ – concentrations of metal ions in the initial solution (mg/L), $C_e$ – concentrations of metal ions in the equilibrium cases (mg/L ), $V$ – solution volume (L), $W$ – dry weight of biochar added (g).

### Evaluating equilibrium models

To explain the experimental results of adsorption isotherms, many models have been proposed In the literature. The two most commonly utilized models are Freundlich and Langmuir. The present study made use of both models. The Langmuir model states that uniform adsorption procedures lead to monolayer adsorption occurs on a uniform surface with a limited number of adsorption sites, without adsorbate trans-migration in the surface's plane (Zakaria *et al*., 2021). This is the Equation that forms the Langmuir sorption isotherm (Brishti *et al*., 2023):

$$\frac{Ce}{qe} = \frac{Ce}{qmax} + \frac{1}{qmaxK_L} \tag{3}$$

In addition to being applicable to the formation of a monolayer, the Freundlich isotherm also describes the surface heterogeneity of adsorbed interaction molecules (Chen, 2015). Moreover, this model utilizing log-transformed (Awwad *et al.*, 2013):

$$log\ qe = log\ Kf + \frac{1}{n} log\ Ce \tag{4}$$

The terms $q_{max}$ and $q_e$ refer to the maximum adsorption capacity and the equilibrium adsorption capacity, respectively, measured in milligrams per gram (mg/g). The variables $C_e$ (mg/L), $K_f$ (L/mg), 1/n (mg/g), and $K$ (L/mg) 1/n represent the adsorbate's adsorption capacity, equilibrium concentrations, adsorption rate, and Freundlich constants, which show how successful the adsorption process was.

### Study of adsorption kinetics

According to the pseudo-first-order model, the number of vacant sites closely correlates with the rate of adsorption site occupancy. The linearization of integral form may be represented as follows (Li *et al*., 2010):

$$log(q_e - q_t) = log\ q_e - \frac{K_1}{2.303} t \tag{5}$$

Written as follows is the pseudo-second-order kinetic model (Zhang *et al.*, 2017):

$$\frac{t}{qt} = \frac{1}{K_2\ qe^2} + \frac{1}{qe} \cdot t \tag{6}$$

The adsorption capacities at equilibrium and at time t, ($mg \cdot g^3$), are given by the values qe and qt, respectively. The pseudo-first-order and pseudo-second-order adsorption rate constants are denoted by $K1$ and $K2$, respectively. The time contact is represented by $t$ (min).

## RESULT AND DISCUSSION

### Characterization of Pgh biochar

#### *Surface area and porosity structure of BC*

An activation period of 3 hours during the manufacture of activated carbon leads to an augmentation in pore size and distribution, highlighting the

requirement for an extended heat treatment duration to achieve complete porosity development (Khadiran *et al.*, 2015). Utilizing $H_3PO_4$ during a 3-hour pyrolysis process enhances Pgh, leading to increased surface area and pore volume. The $H_3PO_4$ concentration has a significant effect on the properties of surface area, pore volumes, and pore size distribution of BC. Increasing concentration results due to increase in surface area, as shown in Table 3. The maximum surface area that has been achieved in this study was 691.58 $m^2/g$ with 40 wt.% $H_3PO_4$ concentration at activation temperature of 600 °C for 3 hours. Increased levels of phosphorous compounds reacting with lignocellulosic materials during impregnation and activation stages could lead to this issue (Yakout and Sharaf El-Deen, 2016).

### *XRD*

Study of X-ray diffraction spectrum investigating and quantifying adsorbent materials' crystalline composition is crucial for effective adsorption. Powder X-ray diffraction (XRD) measures adsorbent materials' crystalline concentration, identifies crystalline phases, and determines lattice plane spacing (Afroze and Sen, 2018). Powder X-ray diffraction (XRD) patterns of biochar samples were measured using an XRD-6000 Shimadzu analyzer with Cu Kα ($\lambda$ = 1.5406˚ A) radiation at 40 kV, 30 mA, and continuous scan mode. A scan rate of 1◦min−1 was used to capture X-ray patterns in the range of 2θ = 10–80°. Figure 2 shows XRD examination of $P_{40}$ biochar, displaying three wide peaks at $2\Theta$ = 10°–30°, 40°–45°, and 70°–75°, indicating disordered stacked amorphous carbon rings. X-ray Diffraction can define biochar made from peganum harmala seeds activated with phosphoric acid. The peak at 2 theta value of 25° in XRD patterns indicates amorphous carbon (Chiu and Lin, 2019), whereas peaks at $2\theta$ = 44° indicate holes from carbon degradation along graphic structures (Elmaguana *et al.*, 2018), 79 suggests Biochar has tiny organized graphene sheets (Qu, 2002).

### *EDX*

To identify the chemical elemental and atomic percent present in the raw material and developed biochar, the energy dispersive X-ray (EDX) identification technique was applied. The spectrum plot and atom percent analysis are illustrated in Figure 3 and Table 4 show carbonization and activation improve precursor carbon content from 49.3% to 63.1%. Carbonization raises carbon levels by decomposing non-carbon and volatile components using heat. Ash concentration of biochar is 17.7%.

**Table 3.** Surface area for biochar

| Label | Chemical method | Method conc. (%) | Surface area (BET) $m^2/g$ |
|---|---|---|---|
| P20 | $H_3PO_4$ | 20 | 322.98 |
| P30 | $H_3PO_4$ | 30 | 554.09 |
| P40 | $H_3PO_4$ | 40 | 691.58 |

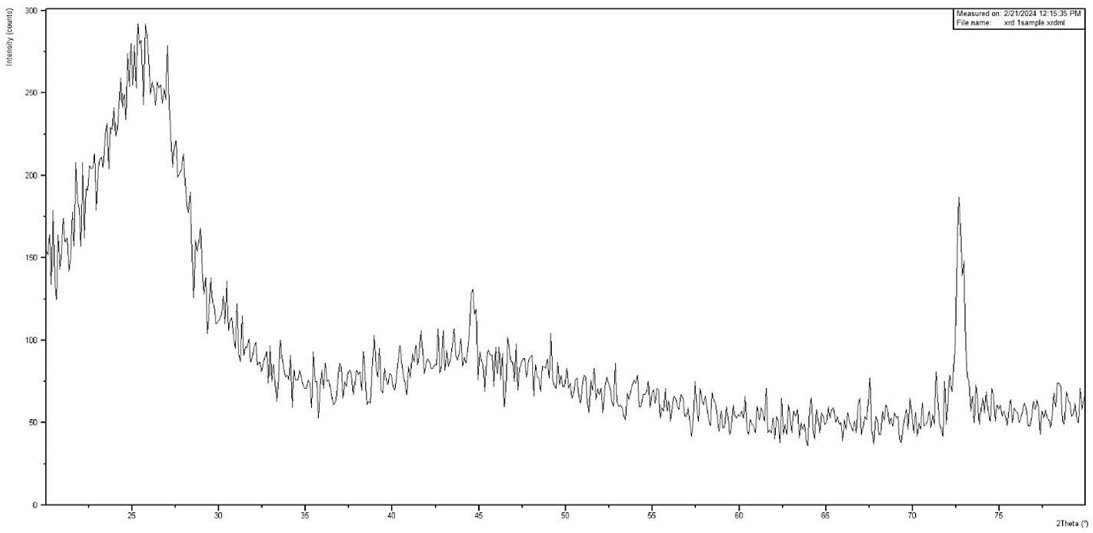


**Figure 2.** XRD for the prepared biochar

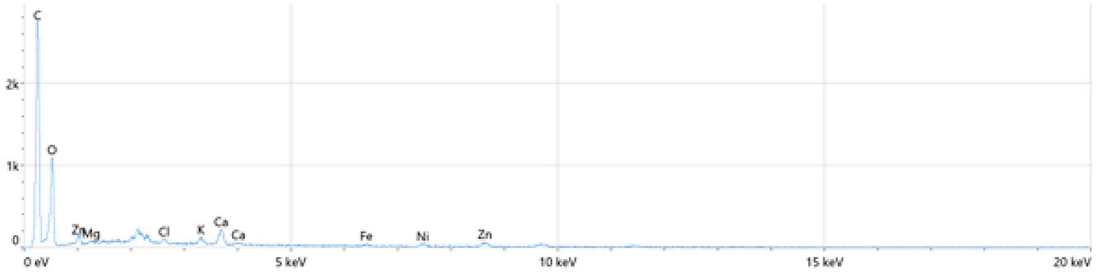


**Figure 3.** The EDX analysis for biochar

**Table 4.** Raw material and biochar elemental composition percentages from EDX evaluation tests

| Element | Atomic % | Atomic % error | Weight % | Weight % error |
|---|---|---|---|---|
| C | 73.1 | 0.6 | 63.1 | 0.5 |
| N | 4.5 | 1.2 | 4.6 | 1.2 |
| O | 16.7 | 0.6 | 19.1 | 0.7 |
| Na | 0.4 | 0.0 | 0.6 | 0.1 |
| P | 4.8 | 0.1 | 10.8 | 0.1 |
| Ca | 0.1 | 0.0 | 0.3 | 0.1 |
| Fe | 0.1 | 0.0 | 0.4 | 0.1 |
| Ni | 0.2 | 0.0 | 1.0 | 0.2 |

### *FTIR*

Pgh's infrared spectroscopy shows these absorption bands: Spectrum peaks at certain wavenumbers: O-H stretching occurs around 3000–3500 $cm^{-1}$ (centered at 3272.59 $cm^{-1}$), alkyl C-H at 2922.78 $cm^{-1}$, aryl-substituted C = C at 1624.33 $cm^{-1}$, alkyl carbonate at 1743.02 $cm^{-1}$, and C-O stretching in acids, alcohols, phenols, ethers, and esters at 1199.16 $cm^{-1}$(Nandiyanto *et al*., 2019). Biochar absorption bands are discovered in many ways via spectroscopy. Unsaturation (C = C-H) and aromatic rings are indicated by 3080.37, terminal alkyne compounds by 2124.05, aryl disulfides by 453.14, secondary amines by 1176.03, carboxylate (carboxylic acid salt) compounds by 1550.02, and aromatic C-H by 752.34 (Lee *et al.*, 2017). Functional group features in precursor and biochar exhibit no hydroxyl (-OH) group peaks after pyrolysis, indicating elimination of this group. Dehydration processes cause most cellulose weight loss before 300 °C. A 200-C-heated cellulose releases $H_2O$ molecules. Unsaturated compounds with C = C bonds' absorption peaks faded and ruptured to create gas or liquid volatiles. Alkene's C-H absorption peaks faded at 500 C because the weak C-H ruptured. This procedure produced gaseous hydrocarbons of tiny molecules like $CH_4$,$C_2H_6$, and $C_2H_4$ (400–500 °C) with reduced hydrogen concentration (Xiao and Yang, 2013). Biochar exhibits C ≡ C stretching in terminal alkyne compounds, aryl disulfides with S-S stretching, and secondary amines with CN stretching, resulting in weakened proton absorption peaks between 900 and 650 $cm^{-1}$ as temperature rises due to C-H rupture and hydrogen formation between 400 and 600 °C. Both charcoal and precursor include carboxylates. Figure 4 shows FTIR raw material and Figure 5 shows FTIR of biochar.

### *SEM*

The material's surface physical morphology was examined using SEM. Figure 6 demonstrate Pgh and Pgh-derived biochar's porous structure from SEM images. Uneven, extremely porous activated carbon surfaces with open, homogeneous macropores on the outer surfaces were found. The biochar has well-developed pores. The development of micropores during carbonization increases the surface area accessible for heavy metal adsorption. $H_3PO_4$ soaked with the precursor likely broke down hemicellulose and lignin, reducing cellulose crystallinity and building high porosity.

### *Pore structure of biochar*

A novel technique for characterizing materials has emerged in recent years: using image processing technologies to examine structure of material data found in SEM pictures. For the

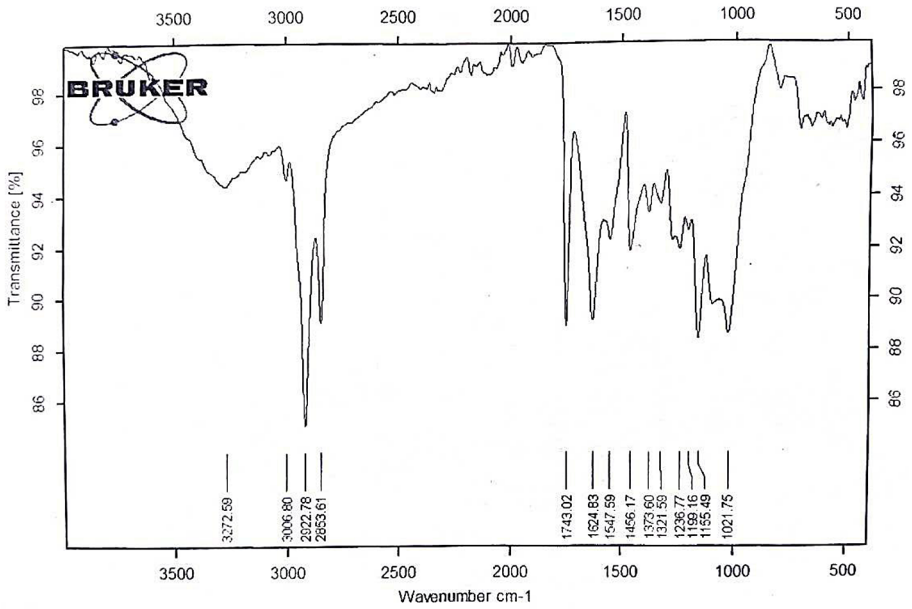


**Figure 4.** FTIR raw material

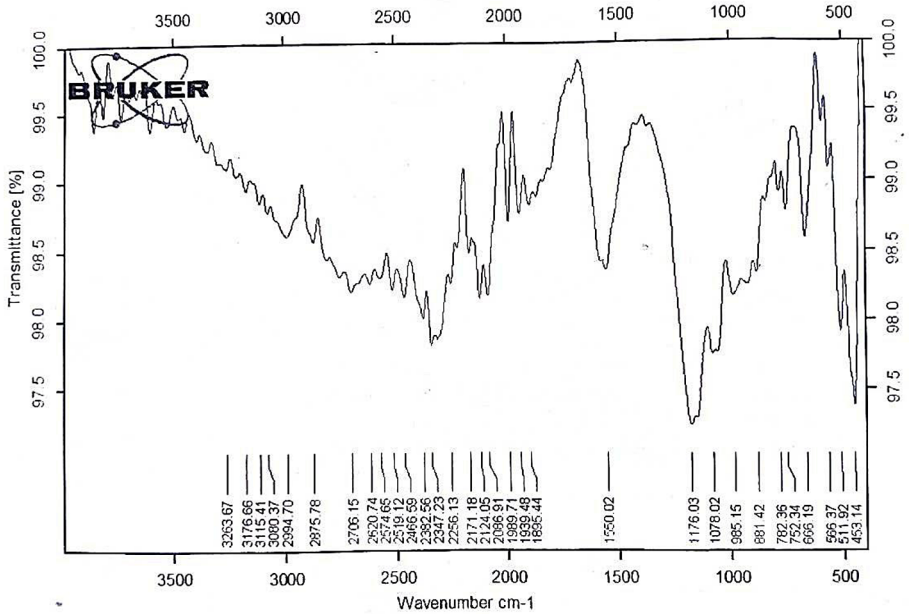


**Figure 5.** FTIR of biochar

purpose of evaluating membrane porosity, Andrzej and his co-worker suggested using computer software SEM image analysis(Mao et al., 2022). Through the use of digital imaging technology and using the box number dimensions approach, Zou and his workmate (Zou *et al.*, 2020) examined coal sample porosity and fractal size. Digital image processing was used by Cardell and his co-workers (Cardell *et al*., 2002) using backscattered electron (BSE) images and X-ray elemental maps to quantify and ascertain the depth of the porous salt medium and porosity. In the last decade well-known researchers (Abdullah *et al*., 2010) provide a technique for using scanning electron microscope (SEM) pictures to determine the pore size distribution of porous materials. To test the approach, a Visual Basic application was built. To separate the picture into bright parts and dark areas – which were presumed to be pores – a threshold value was determined. The threshold value may be ascertained with the use of the cumulative frequency

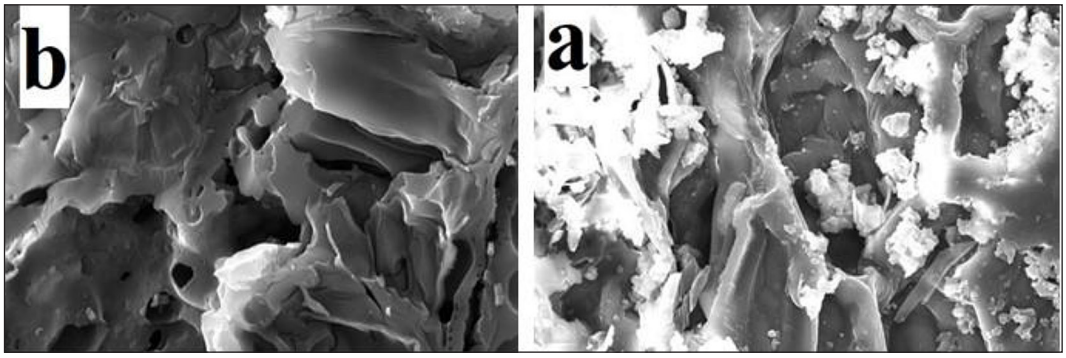


**Figure 6.** Scanning electron microscopy images (MAG: 2000×) and accelerating voltage 30 kV of (a) Peganum harmala seeds (b) Biochar

of the image's pixel intensities. This work uses MATLAB software image analysis to investigate the pore size statistics characterization approach of disordered mesoporous materials based on SEM images. The MATLAB program executes and generates five outputs stored in the main file: four individual images and a composite image summarizing the analysis (similar to the provided example).

### Individual images

- High-resolution (SEM) images – four high-resolution SEM images depict the porous material at various magnifications. SEMs utilize a focused electron beam to image surfaces, suggesting a common origin for these images. Dark regions within the micrographs represent pores within the material.
- Depth map – the second image displays a depth map represented by a color-coded pixel cluster. Variations in pixel intensity likely correspond to surface elevation, with brighter and darker pixels potentially indicating higher and lower elevations, respectively.
- Binary segmentation image – the third image presents a binary segmentation image. Each pixel is classified as either pore space (white) or background (black).
- Pore size distribution – the fourth image displays a pore size distribution graph. This graph depicts the relationship between pore radius (μm) on the x-axis and frequency on the *y*-axis. The observed histogram indicates

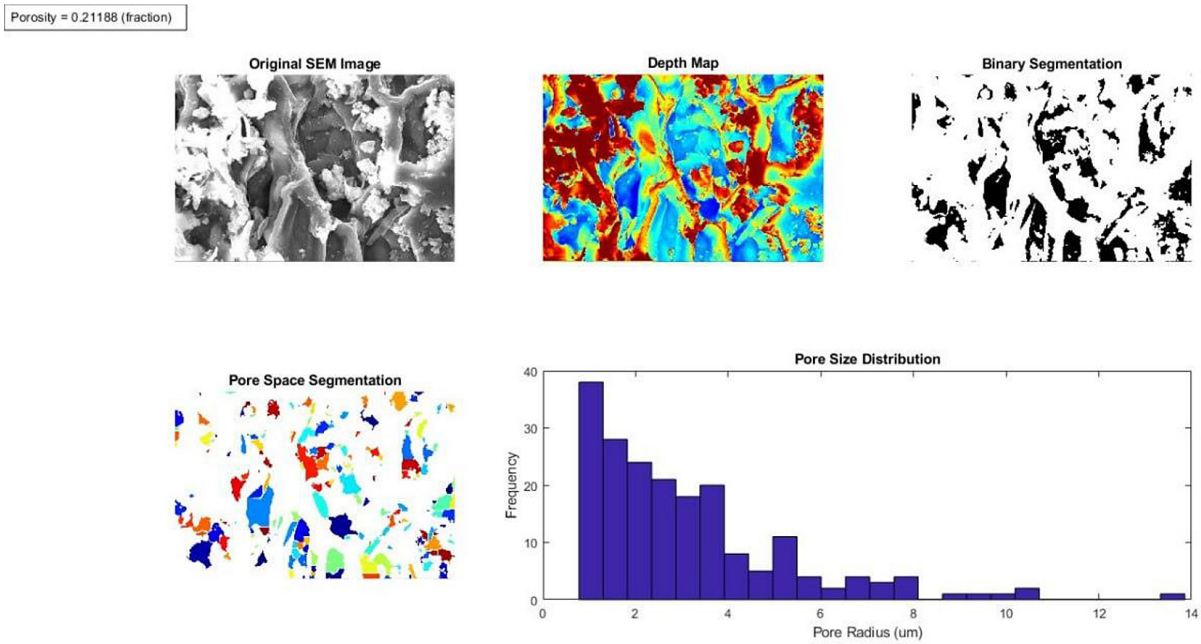


**Figure 7.** Pore structure of Peganum harmala seeds

a prevalence of smaller pores compared to larger ones.

## Porosity calculation

The program calculates the material's porosity, which in this case is 0.27029. Porosity is a material property that quantifies the volume of void space within it. In the context of this analysis, pore space refers to the vacant areas within the material.

## Data validation

For validation purposes, the program performs a comparative analysis of multiple images. This analysis yields results with a high degree of similarity, suggesting consistent and reliable image processing.

## Adsorption variables' effect

### *pH*

The efficiency with which, $Fe^{+3}$, $Ni^{+2}$ and $Pb^{+2}$ ions are removed from water depends on the initial pH of the medium. The equilibrium effect of the initial pH solution on adsorption capacity was studied. Figure 9 shows metal ion elimination at pH 7.0 at 20 ppm heavy metal concentration with adsorbent dosing 0.5 g/L and 440 minutes contact time. From figure it is clearly observed that when the pH has been transformed from 2 to 9, metal ion removal efficiency improved from 12% to 94% for $Fe^{+3}$, 17% to 80.6% for $Ni^{+2}$, and 12.5% to 98% for $Pb^{+2}$. Where the maximum removal has been achieved at pH was 7. While the behavior of removal shows decline in the acidic

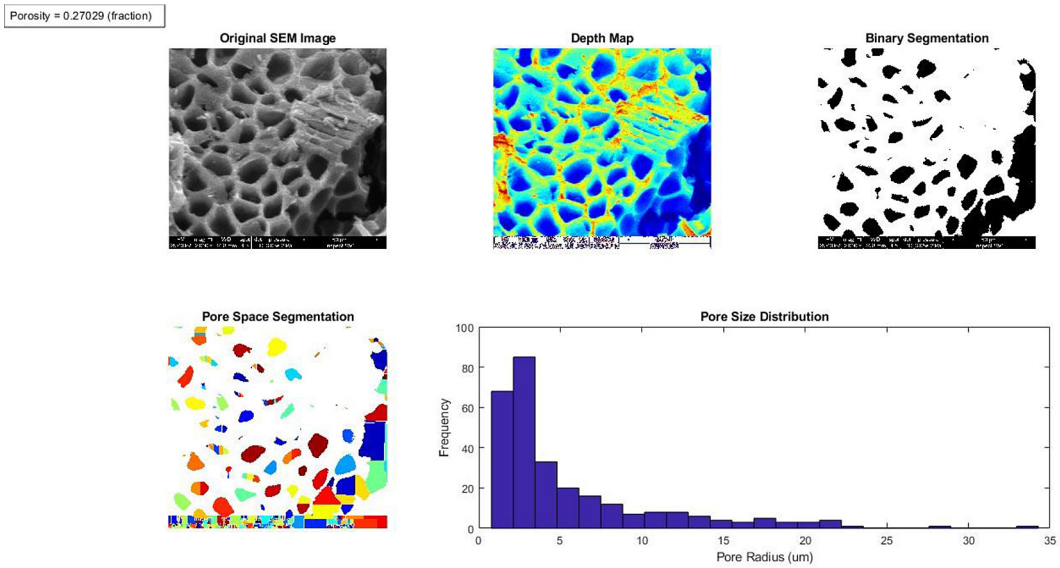


**Figure 8.** Pore structure of biochar

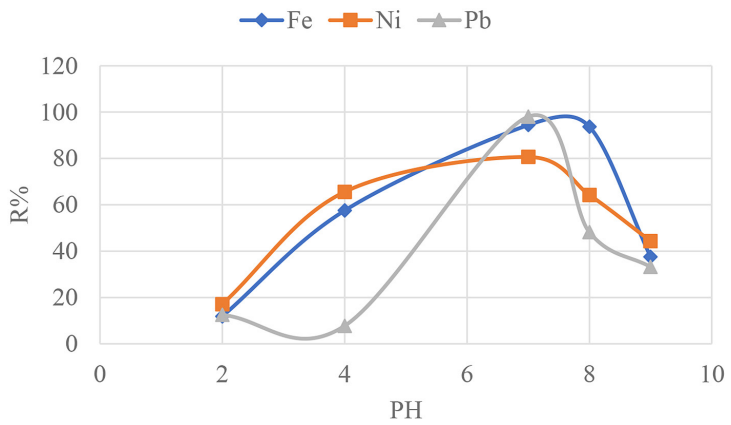


**Figure 9.** Variation of removal percentage with acidity of heavy ions for different ions at initial concentration 20 ppm adsorbent 0.5 g/L and removal time 440 min

medium at pH equals 9. This behavior could be attributed to the possibility of negatively charged metal ions and $H^+$ ions competing diminish as the acidity of the solution (pH) increased. Therefore, the heavy metal ions are the major types that bond to absorbent material. Thus, these results supported by earlier studies (Swelam *et al*., 2018).

### *Initial ions concentration*

The influence of the concentration of different heavy metal ions on the removal percentage are illustrated in Figure 10 at specified pH at 7, adsorbent amount of 0.5 g/L for 440 minutes as contact time. It is evidently revealed from the figure that the removal percentage decreases as the heavy metal ions concentration increased. This phenomena could be clarified as the as metal ions concentration increases, the number of available adsorption sites ready to receive these ions will be reduced, leading to lowering the removal percentage (Brishti *et al.*, 2023).

### *Contact time*

The objective of contact time determination is to find the best time for adsorbing heavy metal ions. Figure 11 illustrates the relation between the removal percent with contact time for $Ni^{+2}$, $Pb^{+2}$, and $Fe^{+3}$ ions. Whereas, other parameters such as adsorbent dose (0.5 g/L), initial pH solution (7) and ions concentration (20 ppm) has been kept fixed. The time duration varies from 5 to 560 minutes. The results show that as the contact time rises, the rate of adsorption initially increases and eventually remains almost constant. Where within the first 200 minutes, the process of adsorption for $Ni^{+2}$, $Pb^{+2}$, and $Fe^{+3}$ took place

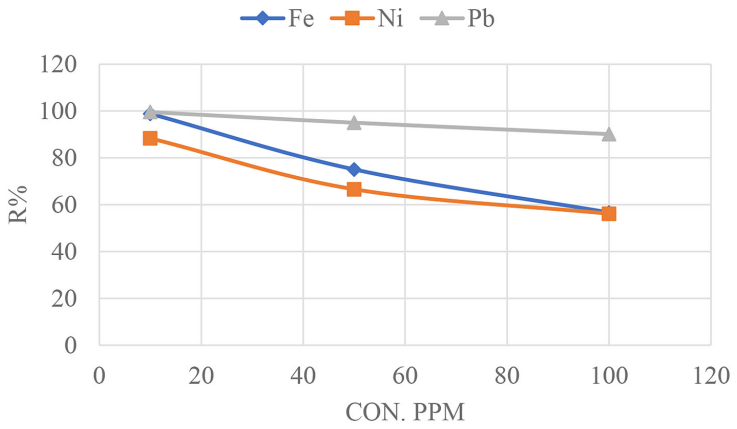


**Figure 10.** Variation of removal percentage with initial concentration of heavy ions for different ions at initial concentration 20 ppm, PH 7 and removal time 440 min

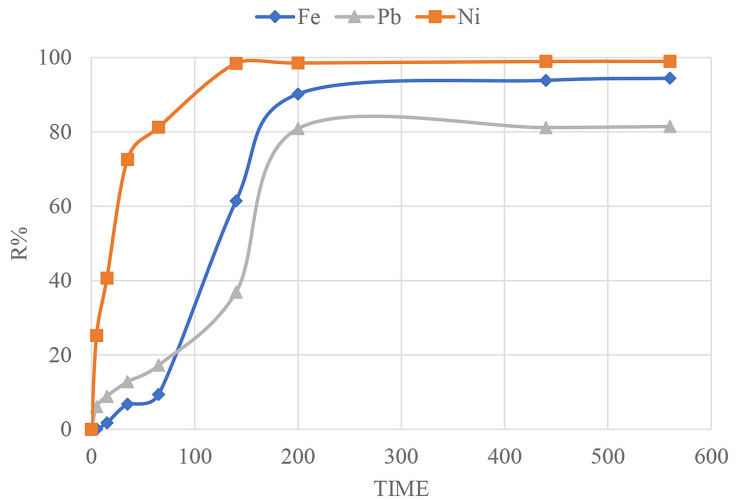


**Figure 11.** Variation of adsorption time with removal percentage of different heavy metal ions at constant pH at 7, adsorbent 0.5 g/L and concentration 20 ppm

swiftly. Nevertheless, after this duration, the adsorption process progressively decelerated until it eventually stabilized after 440 minutes. At that point, it is not possible to extract any further metals from the solution. The highest clearance percentages for $Ni^{+2}$, $Pb^{+2}$, and $Fe^{+3}$ were determined to be 81%, 98.9%, and 94% respectively. This is due to accumulate the heavy ions on adsorption surface With increased contact time, it becomes practically impossible to diffuse further into the adsorbent structure at higher energy sites.

### *Adsorbent dosage*

As increasing the adsorbent amount, while keeping all other parameters same, the removal efficiency first increases, reaches its maximum, and then decreases. The graph illustrates a decrease in the absorption of $Ni^{+2}$ ions as the amount of adsorbent increases. A decrease in the concentration of adsorbent leads to an increase in the number of active sites. As the quantity of adsorbent used is augmented, the particles aggregate, resulting in a decline in both the efficacy and the capacity to eliminate $Ni^{+2}$.

Figure 12 shows demonstrates a significant increase in the removal percentage of $Pb^{+2}$ from 81% to 99.5% when the dose of adsorbent has enlarged from 0.25 to 0.75 g/L. The highest removal percentage has been attained at a dose of 0.75 g/L. The augmentation in the quantity of adsorption sites is directly correlated with the elevated dosage of adsorbent. Therefore, the adsorption sites possess the capacity to capture a larger quantity of ions. During the process of adsorption of $Fe^{+3}$, the percentage of elimination decreased significantly from 99.8% to 55.9%. This is ascribed to When the quantity of activated carbon is substantially increased, there may be an excess of adsorbent material compared to the desired adsorbate molecules. Competitive adsorption may occur when substances other than the intended contaminants occupy the adsorbent sites in the solution or gas stream. Consequently, the total ability to absorb the desired substance may diminish. Maximizing the efficiency and efficacy of activated carbon adsorption systems requires optimization and meticulous dose considerations.

## Evaluation of equilibrium

To understand the nature of adsorption process and interaction of adsorbent surface with metal ions at different concentrations (of 20, 50, and 100 mg/L), an isothermal study was carried out on a P40 sample that was manufactured under certain circumstances (40% acid concentration for 3 hours at 600 °C). The study investigated the adsorption isotherm models for heavy metal adsorption on activated carbon produced from the seeds of Peganum harmala. The models included both monolayer and multilayer adsorption. The predominant isotherm models used for describing the sorption of heavy metal ions on biochar surface are the Langmuir and Freundlich. The Langmuir isotherm may be obtained by plotting the reciprocal of the equilibrium adsorption capacity ($1/q_e$) against the reciprocal of the equilibrium concentration ($1/C_e$). The slope of the graph is determined by adding the maximum adsorption capacity ($q_{max}$) and the Langmuir constant ($K_L$), whereas the y-intercept is the reciprocal of $1/q_{max}$. The $q_{max}$ value, measured in mg/g, represents the maximum ion adsorption capacity of the monolayer. The measure of adsorbent affinity for the BC is computed by $K_L$ (L/mg).

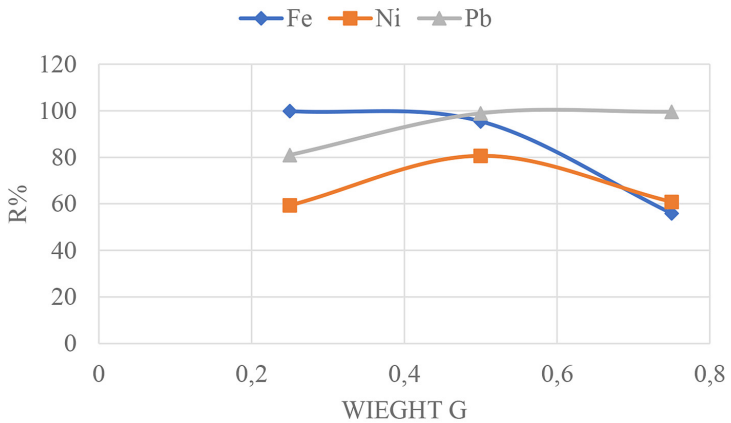


**Figure 12.** Variation of adsorption time with removal percentage of different heavy metal ions at constant pH at 7, concentration 20 ppm and removal time 440 min

Figures 13–15 illustrate the Langmuir isotherm for the adsorption of $Ni^{+2}$, $Pb^{+2}$, and $Fe^{+3}$. The extreme sorption capability of $Pb^{+2}$ is 131.58 mg/g, while the equilibrium constant for the adsorption process is 0.0076 L/mg. The concentration of $Ni^{+2}$ was 103.0928 milligrams per gram and the molar absorptivity was 0.009695 liters per milligram. The $q_{max}$ value for $Fe^{+3}$ was 92.59259 mg/g, while the $K_L$ value was 0.010799 L/mg. The findings are shown in Table 5, Table 6 and Table 7. This might be attributed to the fact that the BC has a surface area of 691.58 $m^2/g$. Greater availability of unoccupied active sites on an expanded surface area enhances the process of ion adsorption. The Langmuir model yielded $R^2$ values of 0.9919, 0.9938, and 0.9914 for the sorption of $Pb^{+2}$, $Ni^{+2}$, and $Fe^{+3}$ onto biochar, respectively. Where, ($K_F$) is the Freundlich isotherm constant and ($n$) is the heterogeneity factor for batch adsorption at equilibrium were determined by graphing the logarithm of the adsorption capacity ($q_e$) against the logarithm of the equilibrium concentration ($C_e$). Figures 16–18 illustrate the Freundlich isotherm for the adsorption of ions on Biochar. The calculated values for the slope and y-intercept are as follows: 0.402 and 1.841 for $Pb^{+2}$, 0.5069 and 1.2121 for $Ni^{+2}$, and 0.291 and 1.5689 for $Fe^{+3}$. The measurement of sorption strength or heterogeneity of surface is determined by the slope value (1/n), which may vary between 0 and 1. Heterogeneity increases as the slope approaches zero. A slope value less than 1/n indicates the presence of a conventional

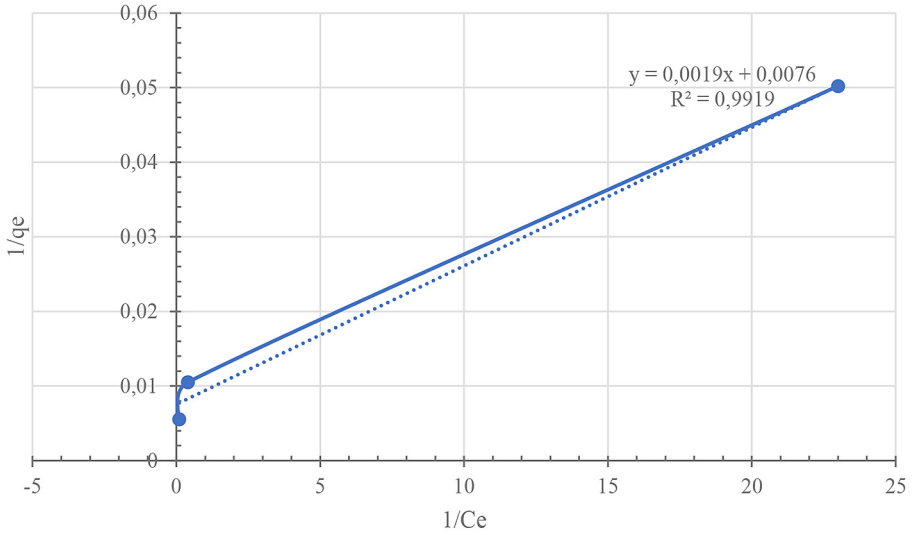


**Figure 13.** Langmuir isotherm for the sorption of $Pb^{+2}$ at constant (dosage 0.5 g/L; solution pH 7and time 440 min)

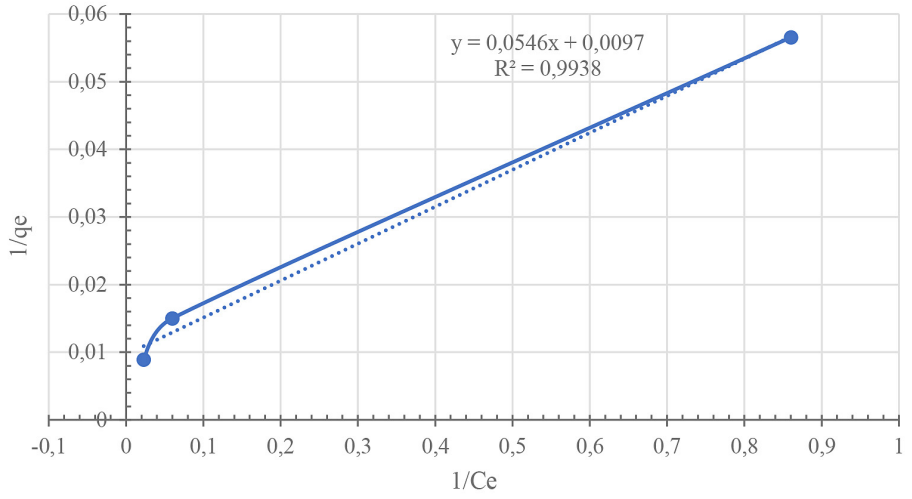


**Figure 14.** Langmuir isotherm for the adsorption of $Ni^{+2}$ (adsorbent dosage 0.5 g/L; initial pH 7; time 440 min)

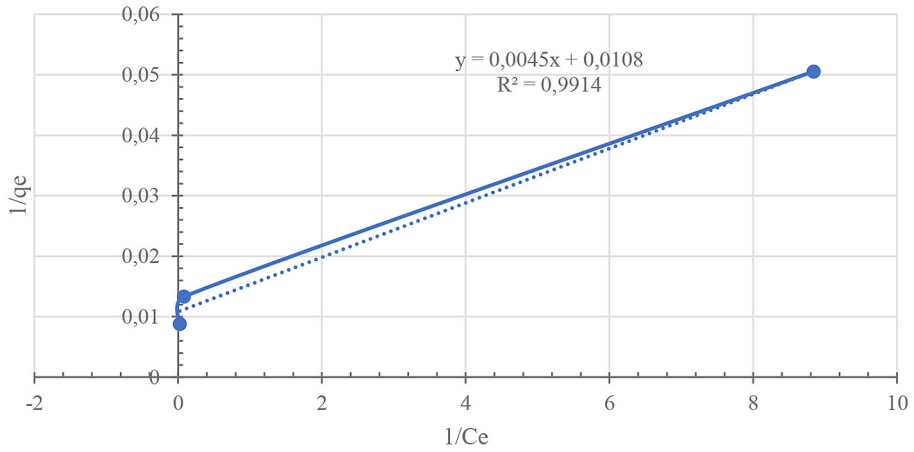


**Figure 15.** Langmuir isotherm for the adsorption of $Fe^{+3}$ (adsorbent dosage 0.5 g/L; initial pH 7; time 440 min)

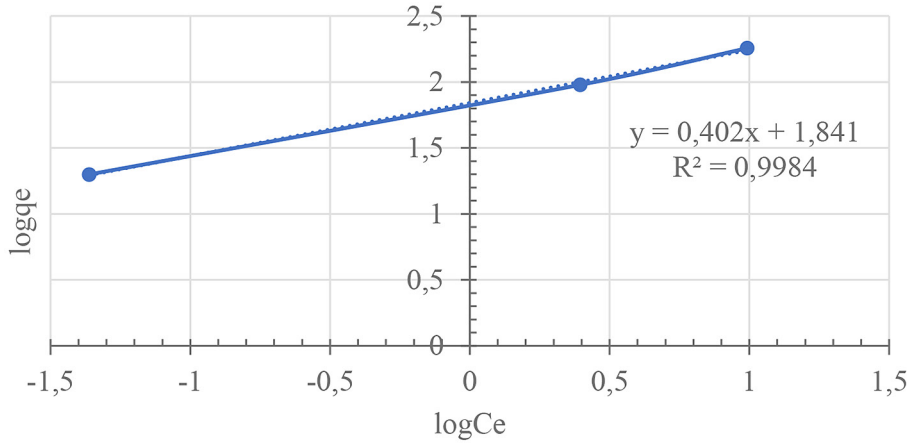


**Figure 16.** Freundlich isotherm for the adsorption of $Pb^{+2}$ (adsorbent dosage 0.5 g/L; initial pH 7; time 440 min)

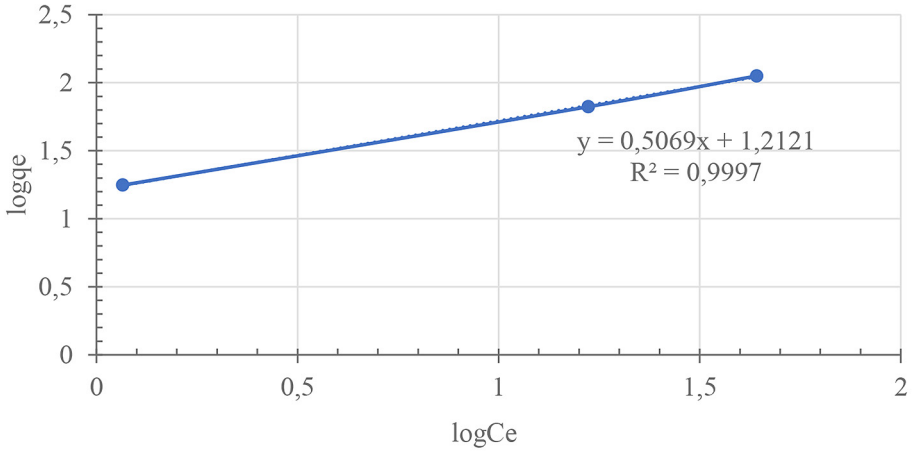


**Figure 17.** Freundlich isotherm for the adsorption of $Ni^{+2}$ (adsorbent dosage 0.5 g/L; Initial pH 7; time 440 min)

Freundlich isotherm, whereas a slope value greater than 1/n indicates cooperative adsorption. The values of n and $K_f$ for $Pb^{+2}$, $Ni^{+2}$, and $Fe^{+3}$ were 69.34258, 16.29671, and 37.05954, respectively, as shown in in Table 5, Table 6 and Table 7. Activated carbon has Freundlich isotherm-like adsorption capacities for $Pb^{+2}$, $Ni^{+2}$, and $Fe^{+3}$, characterized by 1/n values that are less than one. The Freundlich isotherm accurately predicted the adsorption data, as shown

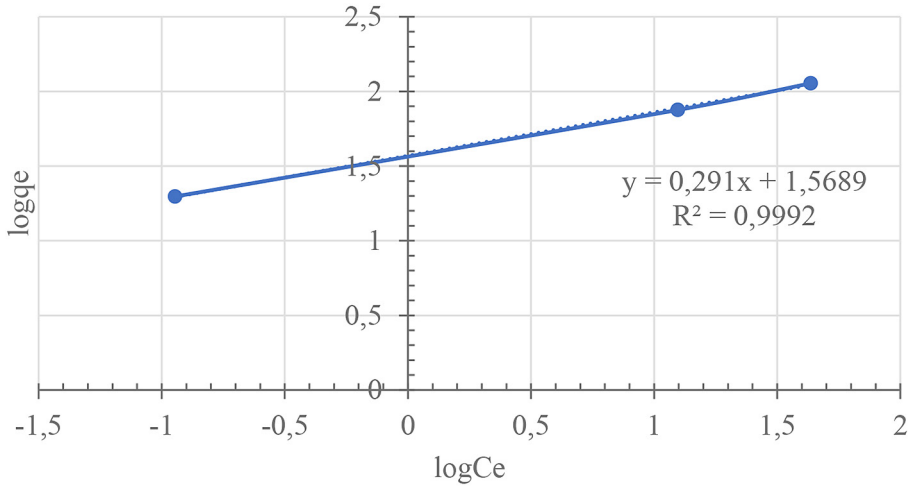


**Figure 18.** Freundlich isotherm for the adsorption of $Fe^{+3}$ (adsorbent dosage 0.5 g/L; onitial pH 7; time 440 min)

**Table 5.** Fitted isotherm models for the adsorption of $Pb^{+2}$ on optimal AC

| Freundlich isotherm | | Langmuir isotherm | |
|---|---|---|---|
| $log\ qe = log\ Kf + \frac{1}{n} log\ Ce$ | | $\frac{1}{qe} = \frac{1}{qmax} + \frac{1}{qmax K_L} \cdot \frac{1}{Ce}$ | |
| *N* | 2.487562 | *q max* | 0.0076 |
| *Kf* | 69.34258 | $K_L$ | 131.5789 |
| *R2* | 0.9984 | *R2* | 0.9919 |

**Table 6.** Fitted isotherm models for the adsorption of $Ni^{+2}$ on optimal AC

| Freundlich isotherm | | Langmuir isotherm | |
|---|---|---|---|
| $log\ qe = log\ Kf + \frac{1}{n} log\ Ce$ | | $\frac{1}{qe} = \frac{1}{qmax} + \frac{1}{qmax K_L} \cdot \frac{1}{Ce}$ | |
| *N* | 1.972775695 | *q max* | 103.0927835 |
| *Kf* | 16.29671235 | $K_L$ | 0.009694865 |
| *R2* | 0.9997 | *R2* | 0.9938 |

**Table 7.** Fitted isotherm models for the adsorption of $Fe^{+3}$on optimal AC

| Freundlich isotherm | | Langmuir isotherm | |
|---|---|---|---|
| $log\ qe = log\ Kf + \frac{1}{n} log\ Ce$ | | $\frac{1}{qe} = \frac{1}{qmax} + \frac{1}{qmax K_L} \cdot \frac{1}{Ce}$ | |
| *N* | 3.436426117 | *q max* | 92.59259259 |
| *Kf* | 37.05953792 | $K_L$ | 0.010799475 |
| *R2* | 0.9992 | *R2* | 0.9914 |

by the high correlation coefficient ($R_2$) values of 0.9984, 0.9997, and 0.9992 for $Pb^{+2}$, $Ni^{+2}$, and $Fe^{+3}$. The Freundlich isotherm model revealed the occurrence of ion multilayer adsorption. The Freundlich isotherm model is often more suitable for describing the adsorption data of ion biosorption onto activated carbon compared to the Langmuir model.

## Kinetics study

Adsorption rate estimates may enhance the comprehension of adsorption processes. The experimental results obtained at various adsorption durations, which indicate variations in adsorption capacity, were analyzed using the pseudo-first order and pseudo-second order equations. The

purpose of this experiment was to evaluate the rate at which $Fe^{+3}$, $lead^{+2}$, and $Ni^{+2}$ ions are absorbed onto P40. The following optimal operating settings were selected for the full-scale batch adsorption process: The initial concentration is 20 parts per million (ppm), the pH is 7, and after 440 minutes, 0.5 grams per liter (g/L) of heavy metal ions have been adsorbed, as shown by the values of qe and qt, respectively. The rate constant for the pseudo-first-order reaction is represented as $k_1$ ($min^{-1}$), whereas the rate constant for the pseudo-second-order adsorption kinetic equation is indicated as $k_2$ [$g\cdot(mg/min)^{-1}$].Both models were assessed for their suitability using a linear plot: the pseudo-first-order model (ln ($q_e$-$q_t$) vs t), and the pseudo-second-order model (($t/q_t$) vs t). Tables 4–6 provide the results of the computations for the four adsorption kinetic models, including the $R_2$ and constant values. These are referenced in Figure 19, Figure 20 and Figure 21. The correlation coefficients for $Fe^{+3}$, $Ni^{+2}$, and $Pb^{+2}$ are 0.8559, 0.9771, and 0.9494, respectively. These values indicate a linear relationship between the variables. However, as seen in Table 8, the pseudo-first-order method fails to fulfill the important criterion of yielding an equal value to the inquiry. The pseudo-second order model is obtained by analyzing the data shown in Figures 22–24. This model

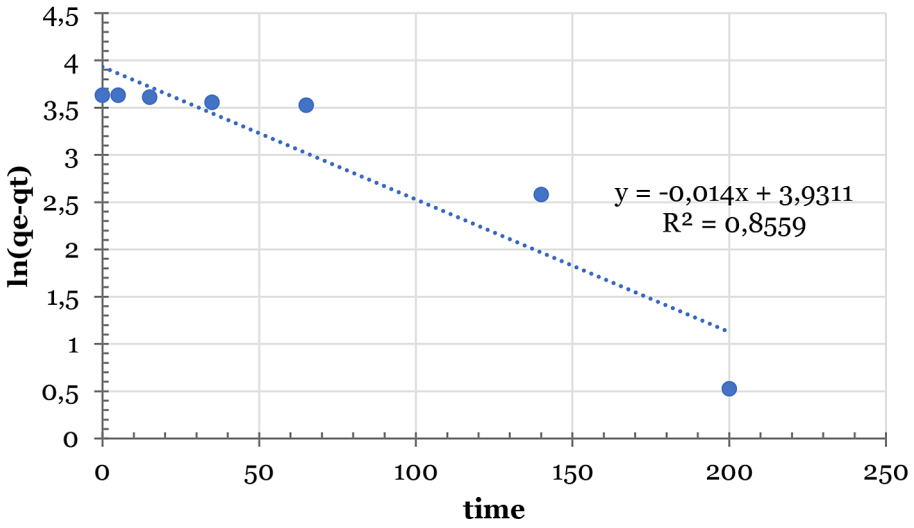


**Figure 19.** Pseudo-first-order for the adsorption of $Fe^{+3}$ (adsorbent dosage 0.5g/L; initial pH 7; concentration 20 ppm)

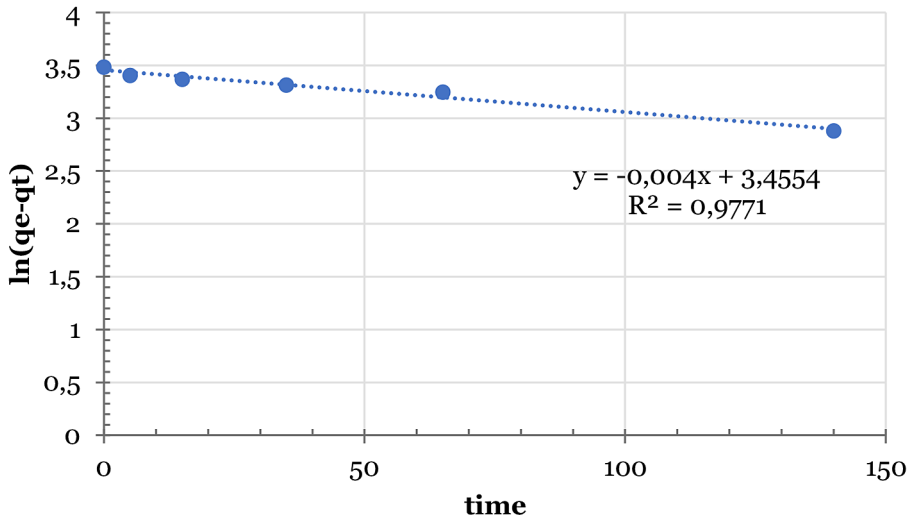


**Figure 20.** Pseudo-first-order for the adsorption of $Ni^{+2}$ (adsorbent dosage 0.5g/L; initial pH 7; concentration 20 ppm

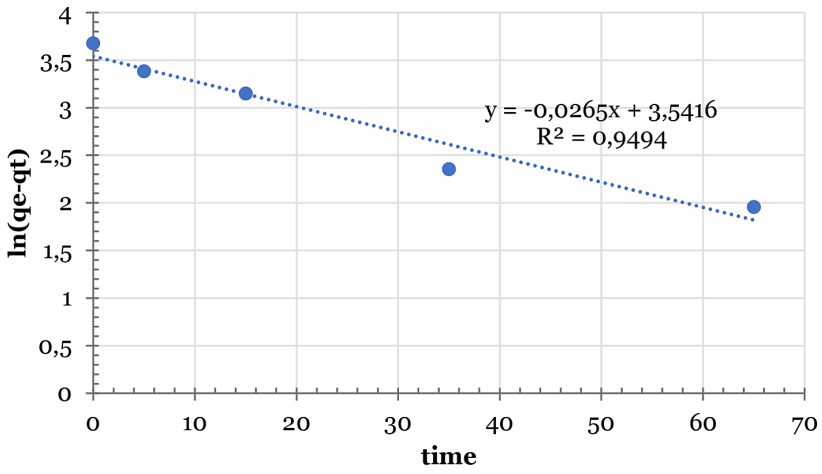


**Figure 21.** Pseudo-first-order for the adsorption of $Pb^{+2}$ (adsorbent dosage 0.5g/L; initial pH 7; concentration 20 ppm

**Table 8.** Kinetic study parameters

| Metal | Parameters | Pseudo-first orde | | Pseudo-second order |
|---|---|---|---|---|
| Fe + 3 | $R^2$ | 0.8559 | k2 | 0.0074 |
| | Constant k1 | 0.014 | | 6.58935E-05 |
| | qe | 37.7737 | | |
| Ni + 2 | $R^2$ | 0.9771 | k2 | 0.7832 |
| | Constant k1 | 0.004 | | 0.000244389 |
| | qe | 32.5818 | | |
| Pb + 2 | $R^2$ | 0.9494 | k2 | 0.9989 |
| | Constant k1 | 0.0265 | | 0.002238492 |
| | qe | 39.5913 | | |

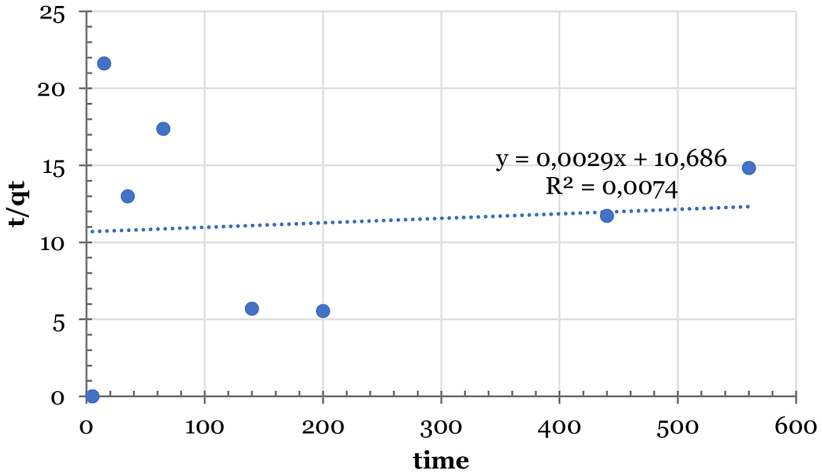


**Figure 22.** Pseudo-second-order for the adsorption of $Fe^{+3}$ (adsorbent dosage 0.5 g/L; Initial pH 7; concentration 20 ppm)

is grounded on the base that the rate of sorption is precisely interrelated to the square of the unoccupied number sites. The data indicate a linear link between $Fe^{+3}$ with a correlation value of 0.0074, $Ni^{+2}$ with a correlation coefficient of 0.7832, and $Pb^{+2}$ with a correlation coefficient of 0.9989. Table 8 demonstrates that the pseudo-second order kinetic model is suitable for the removal of $Pb^{+2}$,

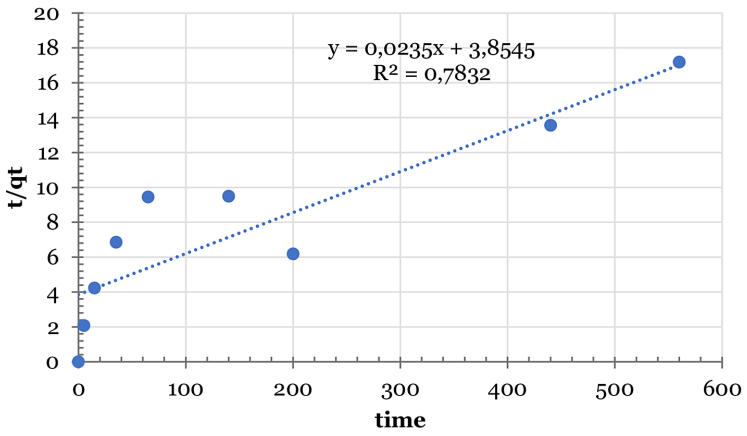


**Figure 23.** Pseudo-second-order for the adsorption of $Ni^{+2}$ (adsorbent dosage 0.5 g/L; Initial pH 7; concentration 20 ppm)

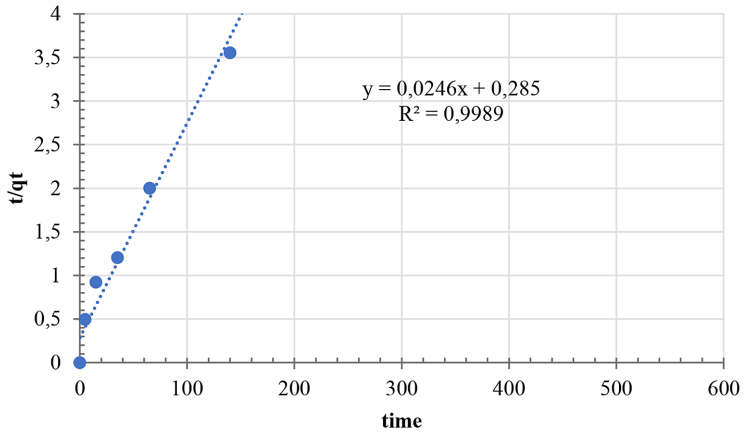


**Figure 24.** Pseudo-second-order for the adsorption of $Pb^{+2}$ (adsorbent dosage 0.5 g/L; initial pH 7; concentration 20 ppm)

**Table 9.** Comparing the adsorption capabilities of various biochar for the adsorption of ions

| Bc from biomass waste materials | Contaminants | Maximum absorption capacity qmax mg/g | References |
|---|---|---|---|
| Corn cobs and luffa sponge | $Fe^{+3}$ | 366.7 | (El-Bendary, El-Etriby and Mahanna, 2021) |
| Olive stone | $Fe^{+2}$<br>$Pb^{+2}$<br>$Cu^{+2}$ | 62.5<br>23.47<br>22.73 | (Alslaibi et al., 2014) |
| Tamarind seeds | $Fe^{+3}$ | 0.019 | (Mopoung et al., 2015) |
| Lapsi seed | $Pb^{+2}$<br>$Ni^{+2}$ | 424<br>70 | (Shrestha et al., 2013) |
| Durian-peel | $Zn^{+2}$<br>$Mg^{+2}$<br>$Pb^{+2}$ | 14.59<br>15.67<br>15.49 | (Wongchuphan et al., 2017) |
| Borassus flabellifer | $Fe^{+3}$ | 33.33 | (Kumar et al., 2021) |
| Rice husk | $Fe^{+3}$<br>$Mn^{+2}$ | 72.2<br>49.6 | (Amer et al., 2021) |
| Date pits | $Fe^{+3}$<br>$Pb^{+2}$<br>$Zn^{+2}$<br>$Co^{+2}$ | 32.17<br>27.5<br>48<br>26.7 | (Awwad et al., 2013) |
| Moringa oleifera | Fe | 8.043 | (Nurul et al., 2012) |
| Doum seed (Hyphaenethebaica) coat | $Ni^{+2}$ | 13.51 | (El-Sadaawy and Abdelwahab, 2014) |

while the pseudo-second order kinetic model is suitable for the removal of $Fe^{+3}$ and $Ni^{+2}$. The physisorption that controlled the process of adsorption is indicated by pseudo-first-order kinetic models, and the chemisorption that controlled the process of adsorption is indicated by pseudo-second order kinetic models. These models adequately represent the adsorption kinetics.

## CONCLUSIONS

This research shows that biochar made from peganum harmala seeds may effectively treat wastewater with $Fe^{+3}$, $Ni^{+2}$, and $Pb^{+2}$ contaminants. Several factors were examined in order to formulate BC. The most effective method for creating micropores was to impregnate the material with 40% phosphoric acid and heat it to 600 °C for three hours. Surface area BET grows as the agent concentration rises up to 40%. The effects of dose, concentration, duration, and pH on the adsorption trials were examined. Wastewater metal ion removal is a breeze using the batch adsorption technique. The equilibrium is reached in the removal efficiency after 440 minutes. Initial solution pH affected batch adsorption of $Fe^{+3}$, $Ni^{+2}$, and $Pb^{+2}$ ions. As the starting concentration of the solutions increased, the adsorption efficiency for $Fe^{+3}$, $Ni^{+2}$, and $Pb^{+2}$ ions also increased. The Freundlich isotherm, which showed multilayer adsorption of $Fe^{+3}$, $Ni^{+2}$, and $Pb^{+2}$ on the BC, is the best fit for the isotherms model of the Activated carbon adsorption of these elements. In the case of $Pb^{+2}$, the kinetics of adsorption have been adequately described by a pseudo-first-order model, which indicates the process was controlled by physisorption. On the other hand, for the removal of $Fe^{+3}$ and $Ni^{+2}$, a pseudo-second-order kinetic model is more appropriate, indicating that the process was controlled by chemisorption. The study's findings suggest that activated carbon made from peganum harmala seeds might be a viable alternative to traditional adsorbents for the removal of $Fe^{+3}$, $Ni^{+2}$, and $Pb^{+2}$ ions from water.

## REFERENCES


1. Abdulmajeed, Y.R., Al-Huda, N. and Mahmood, J. 2018. Production of high surface area activated carbon from grass (Imperata). Iraqi Journal of Chemical and Petroleum Engineering, 19(2), 33–37. Available at: www.iasj.net
2. Afroze, S. and Sen, T.K. 2018. A Review on heavy metal ions and dye adsorption from water by agricultural solid waste adsorbents. Water, Air, and Soil Pollution, 229(7). Available at: https://doi.org/10.1007/s11270-018-3869-z
3. Ajmani, A., Patra, C., Subbiah, S., Narayanasamy, S. 2020. Packed bed column studies of hexavalent chromium adsorption by zinc chloride activated carbon synthesized from Phanera vahlii fruit biomass. Journal of Environmental Chemical Engineering, 8(4), 103825. https://doi.org/10.1016/j.jece.2020.103825
4. Alias, N., Zuki, N.M., Alias, S.H., Kamal, M. 2012. Removal of iron (Fe) by Adsorption using activated carbon *Moringa oleifera* (ACMO) in Aqueous Solution. Jurnal Intelek, 7(2), 22–29.
5. Aljumaili, M.M.N. and Abdul-Aziz, Y.I. 2023. High surface area peat moss biochar and its potential for Chromium metal adsorption from aqueous solutions. South African Journal of Chemical Engineering, 46, 22–34. Available at: https://doi.org/10.1016/j.sajce.2023.06.006
6. Alslaibi, T.M., Abustan, I., Ahmad, M.A., Foul, A.A. 2013. Comparison of activated carbon prepared from olive stones by microwave and conventional heating for iron (II), lead (II), and copper (II) removal from synthetic wastewater. Environmental Progress & Sustainable Energy, 33(4), 1074–1085. https://doi.org/10.1002/ep.11877
7. Ammar, S.H. and Jaafar, S.A. 2017. Adsorption kinetic and isotherms studies of thiophene removal from model fuel on activated carbon supported copper oxide. Iraqi Journal of Chemical and Petroleum Engineering, 18(2), 83–93. Available at: https://doi.org/10.31699/IJCPE.2017.2.7
8. Awwad, N., El-Zahhar, A., Fouda, A., Ibrahium, H. 2013. Removal of heavy metal ions from ground and surface water samples using carbons derived from date pits. Journal of Environmental Chemical Engineering, 1(3), 416–423. https://doi.org/10.1016/j.jece.2013.06.006
9. Brishti, R.S., Kundu, R., Habib, M.A., Ara, M.H. 2023. Adsorption of iron(III) from aqueous solution onto activated carbon of a natural source: Bombax ceiba fruit shell. Results in Chemistry, 5, 100727. https://doi.org/10.1016/j.rechem.2022.100727
10. Cardell, C., Yebra, A., Van Grieken, R.E. 2002. Applying digital image processing to SEM-EDX and BSE images to determine and quantify porosity and salts with depth in porous media. Mikrochimica Acta, 140(1–2), 9–14. https://doi.org/10.1007/s006040200063
11. Chandra, T.C., Mirna, M.M., Sunarso, J., Sudaryanto, Y., Ismadji, S. 2009. Activated carbon from durian shell: Preparation and characterization. Journal of the Taiwan Institute of Chemical Engineers, 40(4), 457–462. https://doi.org/10.1016/j.jtice.2008.10.002
12. Chen, X. 2015 Modeling of experimental adsorption

isotherm data', Information (Switzerland), 6(1), 14–22. Available at: https://doi.org/10.3390/info6010014

13. Chiu, Y.H. and Lin, L.Y. 2019. Effect of activating agents for producing activated carbon using a facile one-step synthesis with waste coffee grounds for symmetric supercapacitors. Journal of the Taiwan Institute of Chemical Engineers, 101, 177–185. Available at: https://doi.org/10.1016/j.jtice.2019.04.050
14. El-Bendary, N., El-Etriby, H.K. and Mahanna, H. 2021. High-performance removal of iron from aqueous solution using modified activated carbon prepared from corn cobs and luffa sponge. Desalination and Water Treatment, 213, 348–357. Available at: https://doi.org/10.5004/dwt.2021.26721
15. Elewa, A., Amer, A., Attalah, M., Gad, H. 2021. Removal of some heavy metals contaminants from aqueous solutions by applying biomass-based modified activated carbon. Egyptian Journal of Chemistry. 64(10), 5929–5944 https://doi.org/10.21608/ejchem.2021.72070.3600Elmaguana Elhadiri, N., Bouchdoug, M., Jaouad, A. 2018. Moroccan Journal of Chemistry Optimization of preparation conditions of activated carbon from walnut cake. Mor. J. Chem. 6(1), 92–105.
16. El-Sadaawy, M. and Abdelwahab, O. 2014. Adsorptive removal of nickel from aqueous solutions by activated carbons from doum seed (Hyphaenethebaica) coat Alexandria Engineering Journal, 53(2), 399–408. Available at: https://doi.org/10.1016/j.aej.2014.03.014
17. Girgis, B.S., Yunis, S.S. and Soliman, A.M. 2002. Characteristics of activated carbon from peanut hulls in relation to conditions of preparation. Materials Letters, 57, 164–172. Available at: www.elsevier.com/locate/matlet
18. Kannan, D., Mani, N. 2014. Removal of Hardness (Ca2+, Mg2+) and Alkalinity from Ground Water by Low Cost Adsorbent using Phyllanthus emblica Wood. International Journal of Chemical and Pharmaceutical Analysis, 1, 208–212. Available at: http://www.ijcpa.in
19. Karagoz, S., Tay, T., Ucar, S., Erdem, M. 2008. Activated carbons from waste biomass by sulfuric acid activation and their use on methylene blue adsorption. Bioresource Technology, 99(14), 6214–6222. https://doi.org/10.1016/j.biortech.2007.12.019
20. Khadiran, T., Hussein, M.Z., Zainal, Z., Rusli, R. 2014. Textural and chemical properties of activated carbon prepared from tropical peat soil by chemical activation method. Bioresources, 10(1). https://doi.org/10.15376/biores.10.1.986-1007
21. Kumar, G., Tonu, N.T., Dhar, P.K., Mahiuddin. 2021. Removal of Fe3+ ions from wastewater by activated borassus flabellifer male flower charcoal. Pollution, 7(3), 693–707. https://doi.org/10.22059/poll.2021.320575.1033
22. Lee, Y., Jo, J., Kim, I., Yoo, Y. 2017. Chemical characteristics and NaCl component behavior of biochar derived from the salty food waste by water flushing. Energies, 10(10), 1555. https://doi.org/10.3390/en10101555
23. Li, Y., Du, Q., Wang, X., Zhang, P., Wang, D., Wang, Z., Xia, Y. 2010. Removal of lead from aqueous solution by activated carbon prepared from Enteromorpha prolifera by zinc chloride activation. Journal of Hazardous Materials, 183(1–3), 583–589. https://doi.org/10.1016/j.jhazmat.2010.07.063
24. Lozano-Castelló, D., Lillo-Ródenas, M., Cazorla-Amorós, D., Linares-Solano, A. 2001. Preparation of activated carbons from Spanish anthracite. Carbon, 39(5), 741–749. https://doi.org/10.1016/s0008-6223(00)00185-8
25. Mao, T., Su, Q. and Cheng, Y. 2022. Statistical method of pore size distribution of disordered mesoporous materials based on electron microscope imaging. Journal of Physics: Conference Series. Institute of Physics. Available at: https://doi.org/10.1088/1742-6596/2321/1/012008
26. Mopoung, S., Moonsri, P., Palas, W., Khumpai, S. 2015b. Characterization and properties of activated carbon prepared from tamarind seeds by KOH activation for Fe(III) adsorption from aqueous solution. ˜the œScientific World Journal/The Scientific World journal, 2015, 1–9. https://doi.org/10.1155/2015/415961
27. Mousa, K.M. and Hadi, H.J. 2016 Coagulation/Flocculation Process for Produced Water Treatment. International Journal of Current Engineering and Technology, 6(2), 551–554. Available at: http://inpressco.com/category/ijcet
28. Mungray, A.A., Kulkarni, S.V. and Mungray, A.K. 2012. Removal of heavy metals from wastewater using micellar enhanced ultrafiltration technique: A review. Central European Journal of Chemistry, 27–46. Available at: https://doi.org/10.2478/s11532-011-0134-3
29. Nandiyanto, A.B.D., Oktiani, R. and Ragadhita, R. 2019. How to read and interpret ftir spectroscope of organic material. Indonesian Journal of Science and Technology, 4(1), 97–118. Available at: https://doi.org/10.17509/ijost.v4i1.15806
30. Prahas, D., Kartika, Y., Indraswati, N., Ismadji, S. 2008. Activated carbon from jackfruit peel waste by H3PO4 chemical activation: Pore structure and surface chemistry characterization. Chemical Engineering Journal, 140(1–3), 32–42. https://doi.org/10.1016/j.cej.2007.08.032
31. Qu Deyang, and S.H. 2002. Studies of the activated carbons used in double-layer supercapacitors, Journal of Power Sources, 109(2), 403–411. Available at: https://doi.org/10.1016/S0378-7753(02)00108-8
32. Radhy, E.D. and Najim, S.T. 2022. Toxicity remediation of petroleum refinery wastewater by electrooxidation techniques using graphite electrode,

in IOP conference series: Earth and Environmental Science. Institute of Physics. Available at: https://doi.org/10.1088/1755-1315/1029/1/012031

33. Razi, M.M., Hishammudin, M.N.M., Hamdan, R. 2017. Factor affecting textile dye removal using adsorbent from activated carbon: a review. MATEC Web of Conferences, 103, 06015. https://doi.org/10.1051/matecconf/201710306015
34. Shrestha, D. and Nyachhyon, A.R. 2021. The effects of different activating agents on the physical and electrochemical properties of activated carbon electrodes fabricated from wood-dust of Shorea robusta, Heliyon, 7(9). Available at: https://doi.org/10.1016/j.heliyon.2021.e07917
35. Shrestha, R.M., Varga, I., Bajtai, J., Varga, M. 2013. Design of surface functionalization of waste material originated charcoals by an optimized chemical carbonization for the purpose of heavy metal removal from industrial waste waters. Microchemical Journal, 108, 224–232. https://doi.org/10.1016/j.microc.2012.11.002
36. Slaiman, Q.J.M., Haweel, C.K. and Abdulmajeed, Y.R. 2010. Removal of heavy metal ions from aqueous solutions using bioconversion on bamboo, Iraqi Journal of Chemical and Petroleum Engineering, 11(3), 23–32.
37. Songrit, J., Ruamsanith, D., Sagnuansakbaramee, N., Wongchuphan, R. 2017. Metal Ion Adsorption using Durian-Peel Activated Carbon, Suratthani Rajabhat Universitry.
38. Swelam, A.A., Sherif, S.S. and Ibrahim, A. 2018. Synthesis and modeling of lead(II) removal from homogeneous and real wastewater by Moringa oleifera seeds. Al Azhar Bulletin of Science, 29(2-A), 105–124.
39. Taseidifar, M., Makavipour, F., Pashley, R.M., Rahman, A.M. 2017. Removal of heavy metal ions from water using ion flotation. Environmental Technology & Innovation, 8, 182–190. https://doi.org/10.1016/j.eti.2017.07.002
40. Timur, S., Kantarli, I.C., Onenc, S., Yanik, J. 2010. Characterization and application of activated carbon produced from oak cups pulp. Journal of Analytical and Applied Pyrolysis, 89(1), 129–136. https://doi.org/10.1016/j.jaap.2010.07.002
41. Tounsadi, H., Khalidi, A., Abdennouri, M., Barka, N. 2016. Activated carbon from Diplotaxis Harra biomass: Optimization of preparation conditions and heavy metal removal. Journal of the Taiwan Institute of Chemical Engineers, 59, 348–358. https://doi.org/10.1016/j.jtice.2015.08.014
42. Tounsadi, H., Khalidi, A., Machrouhi, A., Farnane, M., Elmoubarki, R., Elhalil, A., Sadiq, M., Barka, N. 2016. Highly efficient activated carbon from *Glebionis coronaria* L. biomass: Optimization of preparation conditions and heavy metals removal using experimental design approach. Journal of Environmental Chemical Engineering, 4(4), 4549–4564. https://doi.org/10.1016/j.jece.2016.10.020
43. Widiatmoko, E., Abdullah, M., Khairurrijal, N., Abdullah, M., Khairurrijal, N. 2010. A method to measure pore size distribution of porous materials using scanning electron microscopy images. AIP Conference Proceedings. https://doi.org/10.1063/1.3515554
44. Xiao, R. and Yang, W. 2013. Influence of temperature on organic structure of biomass pyrolysis products. Renewable Energy, 50, 136–141. Available at: https://doi.org/10.1016/j.renene.2012.06.028
45. Xu, J., Chen, L., Qu, H., Jiao, Y., Xie, J., Xing, G. 2014. Preparation and characterization of activated carbon from reedy grass leaves by chemical activation with H3PO4. Applied Surface Science, 320, 674–680. https://doi.org/10.1016/j.apsusc.2014.08.178
46. Yakout, S.M. and Sharaf El-Deen, G. 2016. Characterization of activated carbon prepared by phosphoric acid activation of olive stones. Arabian Journal of Chemistry, 9, S1155–S1162. Available at: https://doi.org/10.1016/j.arabjc.2011.12.002
47. Yang, K., Peng, J., Srinivasakannan, C., Zhang, L., Xia, H., Duan, X. 2010. Preparation of high surface area activated carbon from coconut shells using microwave heating. Bioresource Technology, 101(15), 6163–6169. https://doi.org/10.1016/j.biortech.2010.03.001
48. Yang, K., Peng, J., Srinivasakannan, C., Zhang, L., Xia, H., Duan, X. 2010. Preparation of high surface area activated carbon from coconut shells using microwave heating. Bioresource Technology, 101(15), 6163–6169. https://doi.org/10.1016/j.biortech.2010.03.001
49. Zainab, A.H.A. 2024. Adsorption of dyes from simulated wastewater by activated carbon developed from agricultural materials. [Master's thesis,Al-Nahrain University College of Engineering],Iraq.
50. Zakaria, R., Jamalluddin, N.A., Bakar, M.Z.A. 2021. Effect of impregnation ratio and activation temperature on the yield and adsorption performance of mangrove based activated carbon for methylene blue removal. Results in Materials, 10, 100183. https://doi.org/10.1016/j.rinma.2021.100183
51. Zhang, X., Hao, Y., Wang, X., Chen, Z. 2017. Adsorption of iron(III), cobalt(II), and nickel(II) on activated carbon derived from Xanthoceras Sorbifolia Bunge hull: mechanisms, kinetics and influencing parameters. Water Science & Technology, 75(8), 1849–1861. https://doi.org/10.2166/wst.2017.067
52. Zou, G., She, J., Peng, S., Yin, Q., Liu, H., Che, Y. 2020. Two-dimensional SEM image-based analysis of coal porosity and its pore structure. International Journal of Coal Science & Technology/ International Journal of Coal Science & Technology, 7(2), 350–361. https://doi.org/10.1007/s40789-020-00301-8